Simulation of Ocean Waves Imaging by an Along-Track Interferometric Synthetic Aperture Radar

Mingquan Bao, Claus Brüning, and Werner Alpers

Abstract— A two-dimensional (2-D) model for describing the imaging of ocean waves by an along-track interferometric synthetic aperture radar (AT-INSAR) is derived. It includes the modulation of the normalized radar cross section by the long waves, velocity bunching, and azimuthal image smear due to orbital acceleration associated with long waves and due to the orbital velocity spread within the AT-INSAR resolution cell (parameterized by the scene coherence time). By applying the Monte-Carlo method, AT-INSAR amplitude and phase image spectra are calculated for different sea states and radar configurations. The Monte-Carlo simulations show that velocity bunching affects the AT-INSAR imaging mechanism of ocean waves, and that a unimodal ocean wave spectrum may be mapped into a bimodal AT-INSAR phase image spectrum due to an interference between the velocity term and the velocity bunching term in the AT-INSAR imaging model. It is shown that the AT-INSAR imaging mechanism of ocean waves depends on the ratio of the scene coherence time and the time separation between the observations by the two antennas. If this ratio is larger than one, the AT-INSAR phase image spectra are distorted. Furthermore, the simulations show that the AT-INSAR phase image spectrum is quite insensitive to the ocean wave-radar modulation transfer function. Comparing AT-INSAR with conventional SAR imaging of ocean waves, we find that the azimuthal cut-off in AT-INSAR phase image spectra is shifted toward higher wavenumbers than in conventional SAR image spectra. This implies that AT-INSAR can resolve shorter azimuthal wavenumbers than conventional SAR. Thus we conclude that AT-INSAR phase images are better suited for measuring ocean waves spectra than conventional SAR images.

Index Terms— Along-track INSAR, Monte-Carlo simulation, ocean wave imaging mechanism.

I. INTRODUCTION

THE CONVENTIONAL synthetic aperture radar (SAR) is a high resolution imaging radar which employs a single antenna for transmission and reception of the radar signals. The imaging mechanism of ocean waves by a conventional SAR is determined by the modulation of the normalized radar

cross section (NRCS) by the long ocean waves as well as by motion induced modulations which include velocity bunching and azimuthal image smear [1]–[3]. Unfortunately, it is not possible to separate these modulations in the SAR imaging mechanism of ocean waves. Furthermore, it is difficult to retrieve significant ocean wave heights from conventional SAR data, since the ocean wave-radar modulation transfer function (MTF), which is a poorly known function, enters into the inversion scheme [4], [5].

Recently, airborne along-track interferometric synthetic aperture radars (AT-INSARs) have been developed, which have the potential to measure ocean surface currents, ocean surface waves, and internal waves [6]–[12]. AT-INSARs employ two antennas which are spatially separated by a fixed distance in flight (along track) direction of the platform. The backscattered radar signals from the ocean surface received by the fore and aft antennas are recorded and processed separately into two complex images. Then these two complex images are combined interferometrically into a single complex AT-INSAR image. The phase of the complex AT-INSAR image is approximately proportional to the radial surface velocity field of the imaged ocean scene. Thus, in principle, it is possible to measure the surface velocity field with a spatial resolution equal to the spatial resolution of AT-INSAR.

Marom *et al.* [10] have investigated the AT-INSAR imaging of ocean waves and have retrieved ocean wave spectra from AT-INSAR phase image spectra, but they have neglected velocity bunching and NRCS modulation in their imaging model. Lyzenga and Bennett [13] have derived an expression for the Fourier transform of the complex AT-INSAR image. Milman *et al.* [14] have shown that it is possible to measure both the NRCS modulation and the radial velocity of the sea surface by AT-INSAR. Shemer and Kit [15] have derived an AT-INSAR model which they employed for studying the AT-INSAR imaging of a monochromatic ocean surface waves in the presence of surface currents. Furthermore, Shemer [16] has given an analytical presentation of his model. He [17] has also studied how the NRCS modulation affects the complex AT-INSAR image. Although Shemer has investigated AT-INSAR imaging only for monochromatic waves, his study yields valuable insight into several features of the AT-INSAR imaging mechanism. However, the ocean wave field usually consists of a superposition of harmonic components whose wavelengths and directions vary. Since the AT-INSAR imaging mechanism is often nonlinear, nonlinear interactions may
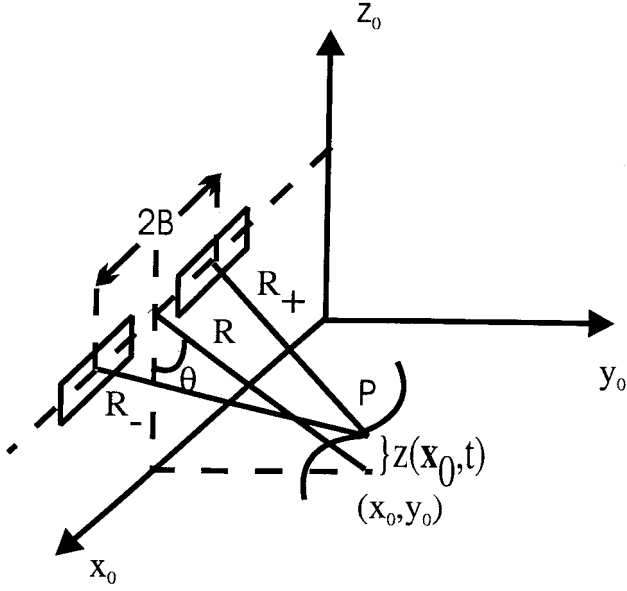
Fig. 1. Schematic of the AT-INSAR geometry.

occur between different wave components. Therefore, realistic simulations of ocean waves imaging by an AT-INSAR require two-dimensional (2-D) ocean wave spectra as input.

The objective of this investigation is to study the imaging mechanism of ocean surface waves by an AT-INSAR. In contrast to the Shemer and Kit's "time dependent" model [15], we derive an AT-INSAR velocity bunching model (Section II). This model includes the NRCS modulation and the modulation induced by the orbital velocity associated with long ocean waves, as well as the degradation in azimuthal resolution induced by the acceleration associated with the long waves and by the motion of the scattering elements (facets) within a AT-INSAR resolution cell, which usually is described by a scene coherence time. In Section III we present results from numerical simulations of AT-INSAR imaging of 2-D ocean wave fields. The AT-INSAR amplitude and phase image spectra are calculated by using the Monte-Carlo method. A series of simulations has been carried out with different radar and ocean wave parameters. These simulations yield good insight into the AT-INSAR imaging mechanism of ocean waves and can be used for explaining effects found previously in measured AT-INSAR phase image spectra. However, in this paper, we only can present a selection of representative simulations. In order to compare our model with the one of Lyzenga and Bennett [13], we also calculate the Fourier transform of the complex AT-INSAR image. Finally, the results are summarized and discussed in Section IV.

II. MODEL FOR AN-INSAR IMAGING OF OCEAN WAVES

The AT-INSAR geometry is depicted schematically in Fig. 1. Here x_0 denotes the coordinate in azimuth (along-track) direction and y_0 the coordinate in ground range (cross-track) direction. The flight direction of the platform carrying the AT-INSAR is in the x_0 direction and the platform velocity is V. The two antennas of the AT-INSAR are separated by a distance $2B$ in along-track direction. The coordinates of a scattering element P on the ocean surface are denoted by $(x_0, y_0, z_0(\mathbf{x_0}, t))$, where $z_0(\mathbf{x_0}, t)$ is the height of ocean surface above the $\mathbf{x_0} = (x_0, y_0)$ plane.

Two operating modes have been proposed for AT-INSAR [6], [18]. In mode 1 the aft antenna transmits radar signals, and both antennas receive the backscattered signals. In mode 2 both antennas transmit and receive the signals.

In mode 2 the fore and aft antennas of AT-INSAR map the same scene with a time separation of $\Delta t = 2B/V$, while in mode 1 they map it with a time separation of $\Delta t = B/V$ [6]. In this paper we consider primarily mode 1, because the AT-INSAR used in the experiment of Marom *et al.* [10] operated in this mode. However, the results derived in this paper can be easily extended to mode 2.

We denote the lengths of the round trip paths from the aft and fore antennas to the scattering element P on the ocean surface at the time t by $R_+(\mathbf{x_0}, t)$ and $R_-(\mathbf{x_0}, t)$, respectively. For the aft antenna this length is given by

$$
\begin{aligned}
R_+(\mathbf{x_0}, t) = 2\{&(x_0 - Vt + B)^2 + y_0^2 \\
&+ [R\cos\theta - z_0(\mathbf{x_0}, t)]^2\}^{1/2} \\
\approx 2R + &\frac{(x_0 - Vt + B)^2}{R} \\
&- 2\cos\theta z_0(\mathbf{x_0}, t)
\end{aligned}
\tag{1}
$$

and for the fore antenna by

$$
\begin{aligned}
R_-(\mathbf{x_0}, t) = \{&(x_0 - Vt + B)^2 + y_0^2 \\
&+ [R\cos\theta - z_0(\mathbf{x_0}, t)]^2\}^{1/2} \\
&+ \{(x_0 - Vt - B)^2 + y_0^2 \\
&+ [R\cos\theta - z_0(\mathbf{x_0}, t)]^2\}^{1/2} \\
\approx 2R + &\frac{(x_0 - Vt + B)^2}{2R} \\
&+ \frac{(x_0 - Vt - B)^2}{2R} - 2\cos\theta z_0(\mathbf{x_0}, t).
\end{aligned}
\tag{2}
$$

Here R denotes the distance from the median of the two antennas to the point $(x_0, y_0, 0)$, and θ the incidence angle.

A. The Signal Received by the Two Antennas of the AT-INSAR

If we assume that the AT-INSAR pulse repetition frequency is much larger than the Nyquist frequency, then the backscattered signal received by the AT-INSAR can be considered as a continuous signal. In this case, the amplitudes of the backscattered signals for the fore and aft antennas $A_-(\mathbf{x_0}, t)$ and $A_+(\mathbf{x_0}, t)$, respectively, are given by

$$
A_\pm(\mathbf{x_0}, t) = r(\mathbf{x_0}, t)\exp[-jk_i R_\pm(\mathbf{x_0}, t)].
\tag{3}
$$

Here k_i denotes the wavenumber of the incoming electromagnetic wave, and $r(\mathbf{x_0}, t)$ the complex reflectivity of the sea surface, which depends on the dielectric constant of ocean water and on the roughness of the ocean surface.

The amplitudes of the backscattered signals received by the two antennas are weighted by the antenna patterns which, for simplicity, we assume to be a Gaussian in azimuth direction [19]

$$
G_\pm(x_0, t) = \exp\left[-\frac{2(x_0 - Vt \pm B)^2}{V^2 T_0^2}\right].
\tag{4}
$$

Here T_0 denotes the AT-INSAR (single-look) integration time.

Thus the signals $S_{\pm}(t, y)$ received by the aft and fore antennas at the time t are given by

$$
\begin{aligned}
S_{\pm}(t, y) &= \int \int A_{\pm}(\mathbf{x_0}, t) G_{\pm}(x_0, t) \delta(y - y_0) dx_0 dy_0 \\
&= \int r(\mathbf{x_0}, t) \exp[-jk_i R_{\pm}(\mathbf{x_0}, t)] \\
&\quad \times \exp\left[-\frac{2(x_0 - Vt \pm B)^2}{V^2 T_0^2}\right] dx_0.
\end{aligned} \tag{5}
$$

In this equation we have replaced, for simplicity, the impulse response function in ground range direction by a Dirac delta function $\delta(y - y_0)$, where y denotes the ground range coordinate in the image plane. Note that in all integrals appearing in this paper the integration extends from $-\infty$ to $+\infty$.

B. The Complex AT-INSAR Image

Like in conventional SAR [19], the signals received by the aft and fore antennas are correlated in the AT-INSAR processor with reference signals. After correlation the signals received by the aft and fore antennas have the form

$$
i_{+}(\mathbf{x}) = \int S_{+}(t, y) \exp\left[j\frac{k_i}{R}(x - Vt + B)^2\right] dt \tag{6}
$$

and

$$
i_{-}(\mathbf{x}) = \int S_{-}(t, y) \exp\left\{j\frac{k_i}{2R}[(x - Vt + B)^2 \right. \\
\left. + (x - Vt - B)^2]\right\} dt \tag{7}
$$

respectively. Here $\mathbf{x} = (x, y)$ denotes the position of the scattering element P in the AT-INSAR image plane. Multiplying $i_{-}(\mathbf{x})$ with the complex conjugate of $i_{+}(\mathbf{x})$ we obtain, after inserting (5) into (6) and (7) and after having carried out the ensemble average, the following expression for the complex AT-INSAR image $I(\mathbf{x})$

$$
\begin{aligned}
I(\mathbf{x}) &= \langle i_{-}(\mathbf{x}) i_{+}^{\star}(\mathbf{x}) \rangle = \int \int \int \int \langle r^{\star}(\mathbf{x_1}, t_1) r(\mathbf{x_2}, t_2) \\
&\quad \times \exp\{jk_i[R_{+}(\mathbf{x_1}, t_1) - R_{-}(\mathbf{x_2}, t_2)]\}\rangle \\
&\quad \times \exp\left[-\frac{2(x_1 - Vt_1 + B)^2}{V^2 T_0^2} - \frac{2(x_2 - Vt_2 - B)^2}{V^2 T_0^2}\right] \\
&\quad \times \exp\left\{-j\frac{k_i}{2R}[(x - Vt_1 + B)^2 - (x - Vt_2 - B)^2]\right\} \\
&\quad dx_1 dx_2 dt_1 dt_2.
\end{aligned} \tag{8}
$$

Here the asterisk denotes the complex conjugate, and the angular brackets denote ensemble averaging. Using (1) and (2), we obtain

$$
\begin{aligned}
R_{+}(\mathbf{x_1}, t_1) &- R_{-}(\mathbf{x_1}, t_2) \\
&= -2\cos\theta[z_0(\mathbf{x_1}, t_1) - z_0(\mathbf{x_1}, t_2)] \\
&\quad + \frac{2B(x_1 - Vt_1) - V(t_1 - t_2)[2x_1 - V(t_1 + t_2)]}{R}.
\end{aligned} \tag{9}
$$

In accordance with many other authors (e.g., [2], [20], [21]), we assume that the backscattered signals from neighboring scattering elements are spatially uncorrelated, but we allow

for a temporal correlation. As in [21], we separate the ocean wave height $z_0(\mathbf{x}, t)$ into two scales, one associated with the long waves and the other with the short waves. Using the Taylor series expansion for long waves and neglecting terms higher than the second order, the displacement of the scattering element within the integration time is approximately equal to the product of the total radial velocity of the scattering element and the time interval $t_1 - t_2$. Thus we can write (see also (A15) of [21])

$$
\begin{aligned}
&\langle r^{\star}(\mathbf{x_1}, t_1) r(\mathbf{x_2}, t_2) \exp\{-2jk_i \cos\theta \\
&\quad \times [z_0(\mathbf{x_1}, t_1) - z_0(\mathbf{x_1}, t_2)]\}\rangle \\
&= \sigma\left(\mathbf{x_1}, \frac{t_1 + t_2}{2}\right) \delta(\mathbf{x_1} - \mathbf{x_2}) \exp\left[-\frac{(t_1 - t_2)^2}{\tau_s^2}\right] \\
&\quad \times \exp\left\{-2jk_i u_{\text{tot}}\left(\mathbf{x_1}, \frac{t_1 + t_2}{2}\right)(t_1 - t_2)\right\}
\end{aligned} \tag{10}
$$

where τ_s denotes the scene coherence time, $\sigma(\mathbf{x_1}, t_2)$ denotes the normalized radar cross section (NRCS), and $u_{\text{tot}}(\mathbf{x_1}, t)$ denotes the total radial velocity of the scattering element. Note that $u_{\text{tot}}(\mathbf{x_1}, t)$ includes the orbital velocity $u_r(\mathbf{x_1}, t)$ associated with the long ocean waves, the surface current velocity, and the phase velocity of the Bragg waves [10], [15]. Here we investigate only the effect of the spatially variable radial orbital velocity on the AT-INSAR imaging mechanism and neglect the contributions from the current velocity and the phase velocity of the Bragg waves, which we assume to be constant. Therefore, in the following, we replace $u_{\text{tot}}(\mathbf{x_1}, t)$ by $u_r(\mathbf{x_1}, t)$. After inserting (9) and (10) into (8), we obtain

$$
\begin{aligned}
I(\mathbf{x}) &= \langle i_{-}(\mathbf{x}) i_{+}^{\star}(\mathbf{x}) \rangle \\
&= \int \int \int \int \sigma\left(\mathbf{x_1}, \frac{t_1 + t_2}{2}\right) \delta(\mathbf{x_1} - \mathbf{x_2}) \\
&\quad \times \exp\left\{-2jk_i u_r\left(\mathbf{x_1}, \frac{t_1 + t_2}{2}\right)(t_1 - t_2)\right\} \exp\left\{-\frac{(t_1 - t_2)^2}{\tau_s^2}\right\} \\
&\quad \times \exp\left\{jk_i \frac{2B(x_1 - Vt_1) - V(t_1 - t_2)[2x_1 - V(t_1 + t_2)]}{R}\right\} \\
&\quad \times \exp\left\{-\frac{2(x_1 - Vt_1 + B)^2}{V^2 T_0^2} - \frac{2(x_2 - Vt_2 - B)^2}{V^2 T_0^2}\right\} \\
&\quad \times \exp\left\{-j\frac{k_i}{2R}[(x - Vt_1 + B)^2 - (x - Vt_2 - B)^2]\right\} \\
&\quad dx_1 dx_2 dt_1 dt_2.
\end{aligned} \tag{11}
$$

Making the substitution $t_1 + t_2 \to 2T_1$ and $t_1 - t_2 \to \tau_1$, and carrying out the integration over x_2 and τ_1, we obtain the following expression for the complex AT-INSAR image

$$
\begin{aligned}
I(\mathbf{x}) &= T_a \pi^{1/2} \exp\left\{-\frac{4B^2}{V^2 T_0^2}\right\} \int \int \sigma(\mathbf{x_0}, T_1) \\
&\quad \times \exp\left\{\left[j\frac{k_i V}{R}\left(x - x_0 - \frac{R}{V}u_r(\mathbf{x_0}, T_1)\right) + \frac{2B}{VT_0^2}\right]^2 T_a^2\right\} \\
&\quad \times \exp\left[-\frac{2jk_i B}{R}(x - x_0)\right] \exp\left\{-\frac{4(x_0 - VT_1)^2}{V^2 T_0^2}\right\} \\
&\quad dx_0 dT_1.
\end{aligned} \tag{12}
$$

In (12) we have replaced the integration variable $\mathbf{x_1}$ by $\mathbf{x_0}$. The time T_a is the effective integration time defined by

$$\frac{1}{T_a^2} = \frac{1}{\tau_s^2} + \frac{1}{T_0^2} \qquad (13)$$

which is always smaller than the integration time T_0, because the backscattering radar signals from the ocean surface are never completely coherent ($\tau_s \neq \infty$) [15].

Equation (12) is the fundamental equation of this paper which describes the time dependent AT-INSAR ocean wave imaging model. In this model $u_r(\mathbf{x_0}, T_1)$ and $\sigma(\mathbf{x_0}, T_1)$ vary with position $\mathbf{x_0}$ as well as with time T_1.

C. The AT-INSAR Velocity Bunching Model

The time dependent AT-INSAR ocean wave imaging model described by (12) can be simplified to an AT-INSAR velocity bunching model. The procedure is the same as described by Plant [22] who has simplified the conventional SAR ocean wave imaging model to a velocity bunching model. If the SAR integration time T_0 is small compared to the period of the dominant ocean wave, then $\sigma(\mathbf{x_0}, T_1)$ and $u_r(\mathbf{x_0}, T_1)$ vary only little during the integration time T_0. In this case the last exponential function appearing in (12), $\exp\{-\frac{4(x_0 - V T_1)^2}{V^2 T_0^2}\}$, decreases rapidly as a function of T_1 for $T_1 \neq x_0/V$. As a result, the time dependent variable $u_r(\mathbf{x_0}, T_1)$ contributes to the image formation only if T_1 is close to x_0/V. Therefore we may expand the radial velocity $u_r(\mathbf{x_0}, T_1)$ linearly around x_0/V in the ocean plane and obtain

$$u_r(\mathbf{x_0}, T_1) = u_r(\mathbf{x_0}) + a_r(\mathbf{x_0})\left(T_1 - \frac{x_0}{V}\right) \qquad (14)$$

where $a_r(\mathbf{x_0})$ denotes the radial component of the orbital acceleration. Note that this expansion differs from the expansion of Plant [22]. He has expanded the radial orbital velocity $u_r(\mathbf{x_0}, T_1)$ incorrectly around x/V in the SAR image plane [23]. Furthermore, we replace the time dependent value $\sigma(\mathbf{x_0}, T_1)$ by its average value $\sigma(\mathbf{x_0})$ during the integration time [24]. Substituting (14) into (12) and carrying out the integration over the time variable T_1, we obtain, after some tedious but elementary mathematics, the following expression for the complex AT-INSAR image

$$I(\mathbf{x}) = \frac{\pi T_0^2 \rho_a}{2} \exp\left[-\frac{4B^2}{V^2 T_0^2}\right] \int \frac{\sigma(\mathbf{x_0})}{\rho_a'(\mathbf{x_0})}$$

$$\times \exp\left[-2jk_i\frac{B}{V}u_r(\mathbf{x_0})\right] \exp\left[\frac{4B^2\rho_a^2}{\rho_a'^2(\mathbf{x_0})T_0^2 V^2}\right]$$

$$\times \exp\left\{\frac{2jBk_i}{R}\left(\frac{2\rho_a^2}{\rho_a'^2(\mathbf{x_0})} - 1\right)\left(x - x_0 - \frac{R}{V}u_r(\mathbf{x_0})\right)\right\}$$

$$\times \exp\left\{-\frac{\pi^2}{\rho_a'^2(\mathbf{x_0})}\left(x - x_0 - \frac{R}{V}u_r(\mathbf{x_0})\right)^2\right\}dx_0. \qquad (15)$$

Here $\rho_a'(\mathbf{x_0})$ denotes the degraded single-look azimuthal resolution which is given by

$$\rho_a'(\mathbf{x_0}) = \left\{\rho_a^2 + \left[\frac{\pi}{2}\frac{T_0 R}{V}a_r(\mathbf{x_0})\right]^2 + \frac{\rho_a^2 T_0^2}{\tau_s^2}\right\}^{1/2}. \qquad (16)$$

In this equation $\rho_a = \lambda_i R/(2VT_0)$ is the full-bandwidth, single-look azimuthal resolution for stationary targets, where λ_i denotes the radar wavelength.

If the distance of two AT-INSAR antennas is set equal to zero, then the phase terms in (15) disappear, and the conventional SAR model is retrieved (see [1], [26]).

III. MONTE-CARLO SIMULATIONS

In this section we present results of Monte-Carlo simulations carried out by using the velocity bunching model as described by (15). This method was first used by Alpers [25] for studying the SAR imaging of a one-dimensional (1-D) ocean wave and later extended by Brüning *et al.* [26] for studying the SAR imaging of a 2-D ocean wave field. Here it is applied for studying the imaging of a two-dimensional ocean field by an AT-INSAR operating in mode 1.

A. The Monte-Carlo Method

Individual AT-INSAR phase and amplitude images are computed pixel-by-pixel (here: 128 × 128 pixels, pixel spacing: 10.0 m) by using (15). For comparison, also the conventional SAR image is calculated using the computer code of Brüning *et al.* [26]. The wave field is generated by a superposition of a finite number of harmonic wave components from a 2-D ocean wave spectrum as described in detail in [26]. Each Fourier component is generated by a Gaussian random number generator. The variance of the random numbers is normalized by the energy contained in each spectral bin of the ocean wave spectrum. Both, the conventional SAR and AT-INSAR image spectra, are obtained by averaging the individual spectra over 50 realizations of ocean wave field. The final simulated spectra are then smoothed over 3 × 3 spectral grid points using a triangle filter.

The modulation of the NRCS due to the long ocean waves is described by a linear ocean wave-radar modulation transfer function (MTF) which includes tilt, hydrodynamic and range bunching modulation. In our simulations we have used the "theoretical" MTF as given in [27]. The two-dimensional ocean wave spectrum $E(\mathbf{k})$ is modeled by a JONSWAP spectrum with a frequency dependent spreading factor [26]. The input ocean wave spectra are corrected for scanning distortions as discussed in [27]. The Monte-Carlo simulations have been carried out for a large number of ocean wave spectra and radar parameters. In the following we present some representative results of these simulations.

B. AT-INSAR Imaging of Swell Traveling in Different Directions

For describing swell we have used a highly peaked JON-SWAP spectrum with the parameters given in Table I. The radar and flight parameters used in the simulations are given in Table II. The AT-INSAR imaging of swell is studied as a function of azimuthal angles ϕ_p (angle relative to the flight direction). In these simulations the scene coherence time is set equal to 0.12 s. Figs. 2–6 show the results of the simulations where the dominant ocean wave (as given by the spectral peak) travels at $\phi_p = 90°, 60°, 10°, 5°$, and $0°$, respectively. Note
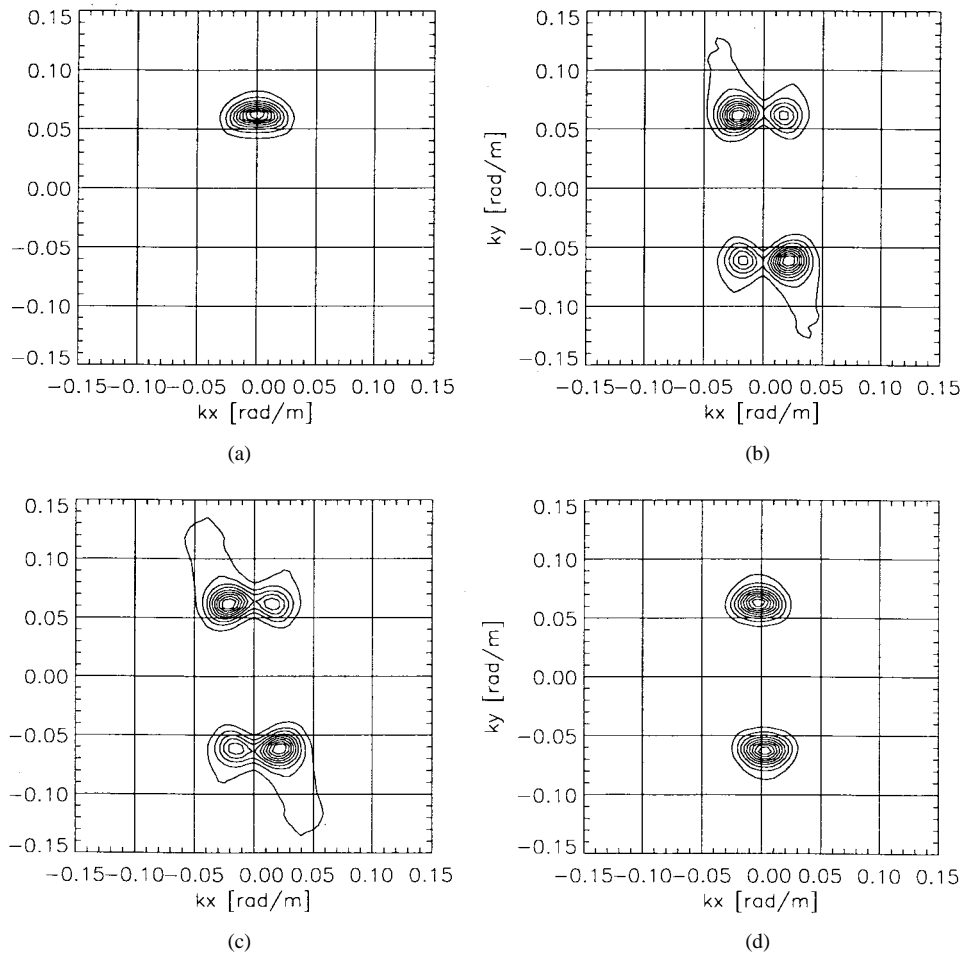
Fig. 2.   (a) Ocean wave spectrum with $\phi_p = 90°$ (range traveling waves), (b) conventional SAR image spectrum, (c) AT-INSAR amplitude image spectrum, and (d) AT-INSAR phase image spectrum simulated from the ocean wave spectrum shown in (a).

<div style="text-align:center">

TABLE I
JONSWAP SPECTRAL PARAMETERS USED IN
THE SIMULATIONS FOR DESCRIBING SWELL

</div>

Phillips parameter α	0.000212
Peak enhancement factor γ	10.0
Significant wave height H_s, m	0.6
Peak wavelength λ_p, m	100

<div style="text-align:center">

TABLE II
THE RADAR AND FLIGHT PARAMETERS USED IN THE SIMULATIONS

</div>

Range distance, m	15000
Aircraft velocity, m/s	200
Incidence angle, deg	45
Azimuthal resolution, m	12.0
Integration time, s	0.751
Distance between the two antennas, m	19.6
Radar wavelength, m	0.24
Polarization	VV
Number of looks	1

that in all contour plots shown in this paper, the contour lines represent nine equally spaced levels.

Fig. 2(a) shows the swell spectrum where the dominant wave of wavelength of 100 m travels in range direction ($\phi_p = 90°$). The conventional SAR image spectrum simulated from

this wave spectrum is shown in Fig. 2(b). Due to the well known interference between velocity bunching and NRCS modulation, a unimodal ocean wave spectrum may be mapped into a bimodal conventional SAR image spectrum, as discussed in detail in [24]. Due to the same interference, AT-INSAR maps this unimodal ocean wave spectrum into a bimodal AT-INSAR amplitude image spectrum [see Fig. 2(c)]. Fig. 2(d) shows the corresponding AT-INSAR phase image spectrum which is simulated from the same ocean wave spectrum. Note that the AT-INSAR phase image spectrum, unlike the conventional SAR image spectrum, is unimodal (apart from the 180° ambiguity).

When the dominant wave travels close to the azimuthal direction, e.g., when $\phi_p = 5°$ or $\phi_p = 10°$, then the AT-INSAR phase image spectra are split into two pieces as can be seen from Figs. 4(d) and 5(d). This interesting phenomenon is also evident in data from an experiment carried out with the airborne AT-INSAR of the Jet Propulsion Laboratory (JPL) [10]. This experiment, in which AT-INSAR measurements were performed along two flight tracks whose directions differed by 90°, took place off the coast of Marina California on Sept. 8, 1989. During one flight track, the waves traveled approximately in range direction, while during the other flight track they traveled approximately in azimuthal direction. For
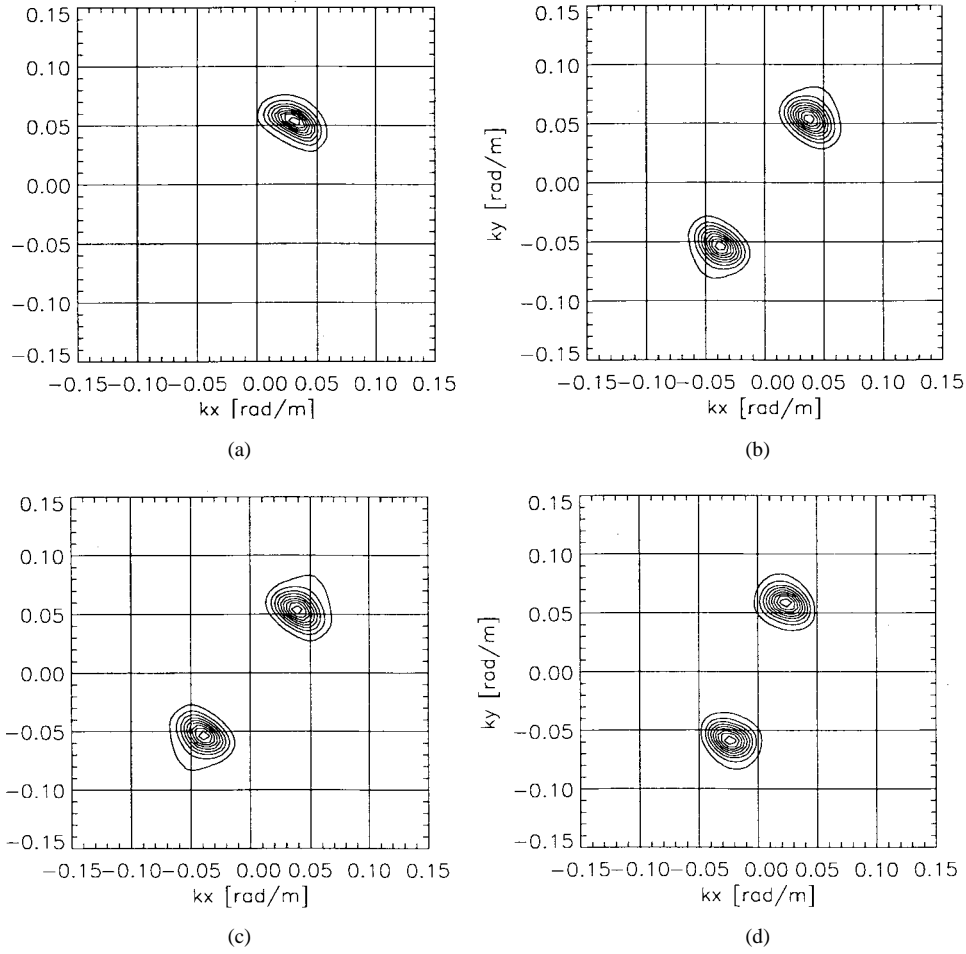
Fig. 3. Same as Fig. 2, but with $\phi = 60°$.

the last flight track, an additional spectral peak was found in the AT-INSAR phase image spectrum. Marom *et al.* [10] stated: "This wave system is visible only in this particular location of the image and most probably is of local nature." However, this statement does not explain satisfactorily why this additional swell system was not imaged when the airplane flew in the other flight track. The *in-situ* measurement of the ocean wave spectrum by a pressure sensor array did not delineate this additional swell system [10]. Based on the simulations described above, we conjecture that this additional spectral peak may be an artifact caused by the AT-INSAR imaging mechanism, which occurs when ocean waves travel near the azimuthal direction.

We now show that the additional peak is the result of the interference of two terms in (15) which causes a splitting of the AT-INSAR phase image spectrum. To this end, we carry out Monte-Carlo simulations where we modify the mapping integral (15). In the first simulation, we set the phase of the first factor in the integrand equal to zero, i.e.,

$$-2k_i \frac{B}{V} u_r(\mathbf{x_0}) = 0 \qquad (17)$$

and keep all other terms unchanged. In the second simulation, we set the phase of the second factor in the integrand equal

to zero, i.e.,

$$\frac{2Bk_i}{R}\left(\frac{2\rho_a^2}{\rho_a'^2(\mathbf{x_0})} - 1\right)\left(x - x_0 - \frac{R}{V}u_r(\mathbf{x_0})\right) = 0 \qquad (18)$$

and keep all other terms unchanged. We call the terms (17) and (18) velocity and velocity bunching terms, respectively, since the first term is proportional to the orbital velocity and the second term contains the factor, $x - x_0 - \frac{R}{V}u_r(\mathbf{x_0})$, which occurs also in the expression describing velocity bunching in SAR ocean wave imaging models. The results of the simulations for a wave spectrum with an azimuthal angle of the dominant wave of $\phi_p = 10°$ are depicted in Fig. 7(a) and (b). No splitting of the spectrum occurs in these cases. In Fig. 7(a), the peak of the AT-INSAR phase image spectrum has an azimuthal angle of $\phi_p = 15°$, and in Fig. 7(b) it has an azimuthal angle of $\phi_p = 9°$. However, the simulation carried out with the unmodified mapping integral (15), does show a spectral splitting [Fig. 4(d)]. This indicates that an interference between these two terms must be responsible for the spectral splitting. Like for conventional SAR, also for AT-INSAR, the velocity bunching term does not contribute to the AT-INSAR imaging mechanism for range traveling waves. When the waves have an azimuthal component, then both the velocity term and the velocity bunching term contribute to the AT-INSAR imaging mechanism. For certain AT-INSAR
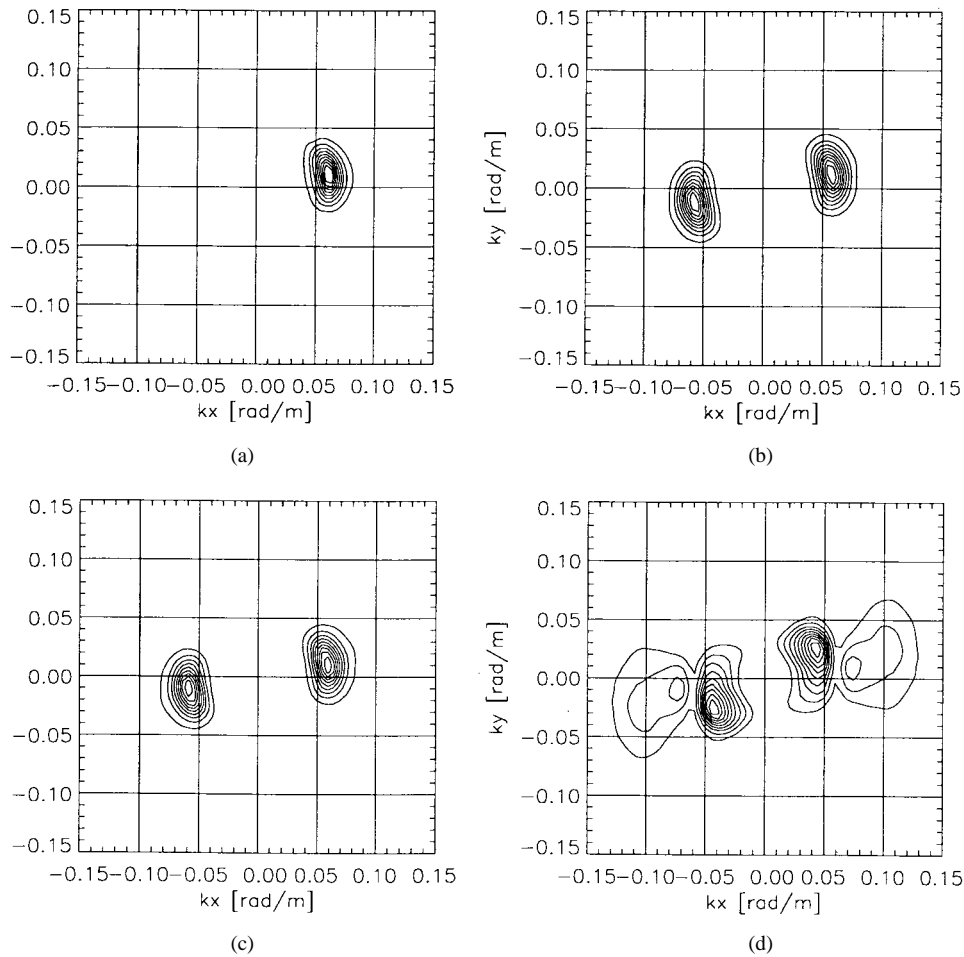
(a)

(b)

(c)

(d)

Fig. 4. Same as Fig. 2, but with $\phi_p = 10°$.

and ocean wave parameters, these two terms may interfere destructively such that the AT-INSAR phase image spectrum is split into two pieces. This effect is similar to the well known interference between velocity bunching and NRCS modulation encountered in the imaging mechanism of ocean waves by a conventional SAR, which can also lead to spectral splitting as discussed in detailed in [24].

C. Variation of the Separation Distance Between the Two Antennas

If the separation distance between the two antennas, 2B is increased and the scene coherence time, τ_s, is kept constant ($\tau_s = 0.12$ s), or equivalently, if the time separation between the observations by the two antennas, $\Delta t = B/V$, is increased such that Δt becomes larger than τ_s, then the signals received by the fore and aft SAR antennas lose coherence. As a result, the AT-INSAR phase image spectrum becomes distorted. This is evident from Fig. 8(a) and (b), where the AT-INSAR phase image spectra for range traveling ocean waves are plotted. They have been calculated from the ocean wave spectrum shown in Fig. 2(a), with (a) $\Delta t = 0.200$ s, $2B = 80$ m; and (b) $\Delta t = 0.225$ s, $2B = 90$ m, respectively. The other parameters used in simulations are the same as before (see Tables I and II).

D. Variation of the Scene Coherence Time

On the other hand, if the separation distance between the two antennas is kept constant (here: $2B = 19.6$ m, $\Delta t = 0.049$ s), but the scene coherence time is decreased, then the AT-INSAR phase image spectrum is also distorted (see Fig. 9). Fig. 9(a) and (b) show AT-INSAR phase image spectra calculated from the ocean wave spectrum plotted in Fig. 2(a), with (a) $\tau_s = 0.03$ s and (b) $\tau_s = 0.04$ s, respectively.

These simulations reveal that AT-INSAR phase image spectra exhibit a strong dependence on τ_s and $\Delta t = B/V$. From these simulations and others not shown here we conclude that the time separation Δt between the observations by the two antennas must be smaller than the scene coherence time in order to avoid distortions in the AT-INSAR phase image spectrum.

E. Variation of the R/V Ratio

As in conventional SAR, also in AT-INSAR imaging of ocean waves, the R/V ratio is an important factor. If the R/V ratio increases, velocity bunching becomes stronger [25], [26] and thus leads to an increase of the nonlinearity of the AT-INSAR imaging mechanism. We have simulated AT-INSAR imaging of swell with different R/V ratios. In the simulations we have chosen the wavelength and propagation direction
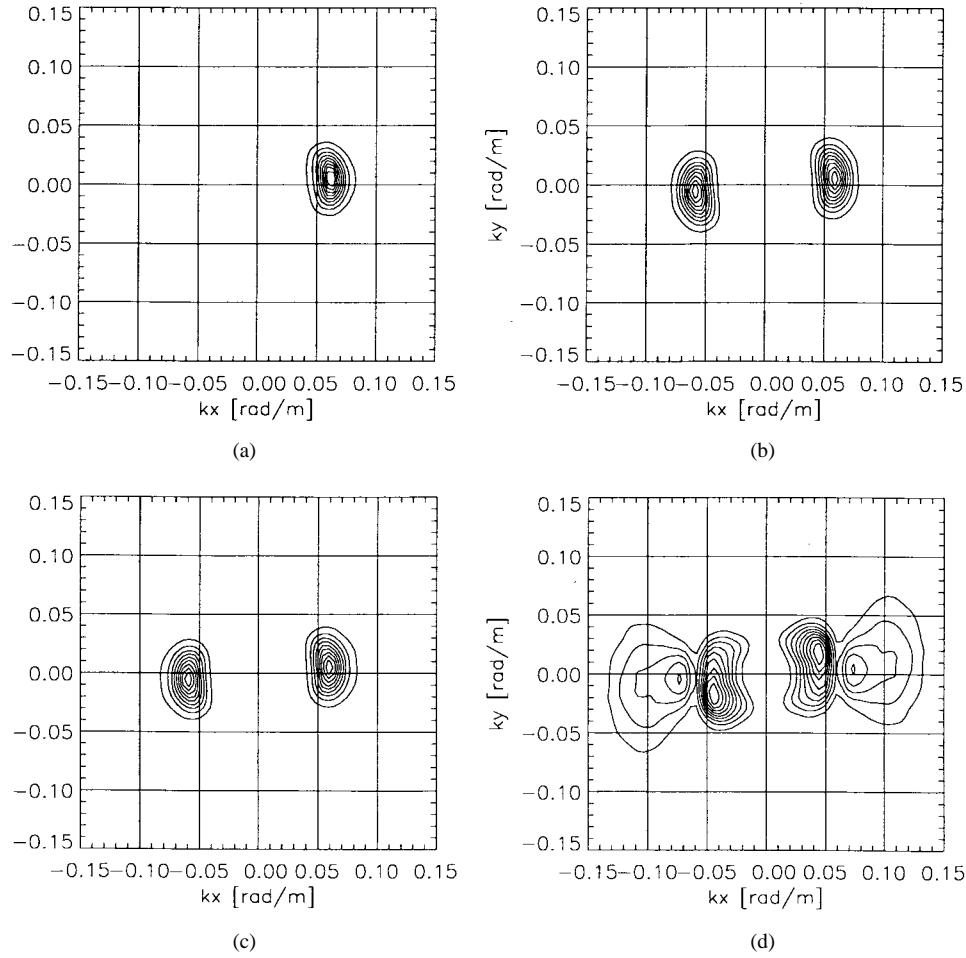
(a)

(b)

(c)

(d)

Fig. 5. Same as Fig. 2, but with $\phi_p = 5°$.

of the dominant wave to be 100 m and 20°, respectively, and the significant waveheight to be 0.6 m. The velocity of platform has been fixed at $V = 200$ m/s, but the range distance between radar and target, R, has been varied: $R = 6\,000$ m, $16\,000$ m, and $18\,000$ m, which yields $R/V = 30$ s, 80 s, and 90 s, respectively. The results of these simulations are depicted in Fig. 10. As can be seen from Fig. 10(b), the mapping is linear for $R/V = 30$ s. The AT-INSAR phase image spectrum is split into two pieces for $R/V = 80$ s and $R/V = 90$ s [Fig. 10(c) and (d)]. In Fig. 10(c) ($R/V = 80$ s) the line of minimum intensity is located at $k_x^{(80)} = \pm 0.055$ rad/m and in Fig. 10(d) ($R/V = 90$ s) at $k_x^{(90)} = \pm 0.042$ rad/m. This shows that the distance between the line of minimum intensity and the k_y-axis decreases when the R/V ratio increases.

F. Variation of the Ocean Wave-Radar Modulation Transfer Function

Now we investigate the effect of the ocean wave-radar modulation transfer function (MTF) on the AT-INSAR phase image spectrum. We have calculated the AT-INSAR phase image spectra first by neglecting the NRCS modulation ($\sigma(\mathbf{x_0}) =$ const.) and then by inserting the "theoretical" MTF into (15). As shown in [1] and [26], the conventional SAR imaging

mechanism is dominated by the NRCS modulation for small R/V ratios (e.g., $R/V = 1.0$ s). However, the AT-INSAR phase imaging mechanism is quite insensitive to the MTF. This does not only apply for small R/V ratios, but also for large R/V ratios, as shown in [28]. Here we have simulated AT-INSAR phase image spectra for a fully developed wind sea by setting R/V in (15) equal to 100 s. For a fully developed wind sea the JONSWAP spectrum reduces to the Pierson-Moskowitz spectrum, if the JONSWAP spectral parameters γ and α are set equal to 1 and 0.0081, respectively. For a wind speed at a height of 10 m $U_{10} = 12$ m/s, the significant waveheight is 3.0 m and the peak wavelength 137.7 m. Fig. 12 shows the AT-INSAR phase image spectra simulated from the Pierson-Moskowitz spectrum plotted in Fig. 11, when the AT-INSAR platform flies parallel [Fig. 12(a) and (b)] and perpendicular [Fig. 12(c) and (d)] to the propagation direction of dominant wave, respectively. The AT-INSAR phase image spectra shown in Fig. 12(a) and (c) have been calculated with a vanishing MTF, and the ones shown in Fig. 12(b) and (d) with the "theoretical" MTF. We see from these simulations that for waves propagating in azimuthal direction the MTF has no effect on the AT-INSAR phase image spectra. However, for ocean waves propagating in range direction, the AT-INSAR phase image spectra calculated with different MTF's differ slightly. From these and other simulations not shown here we
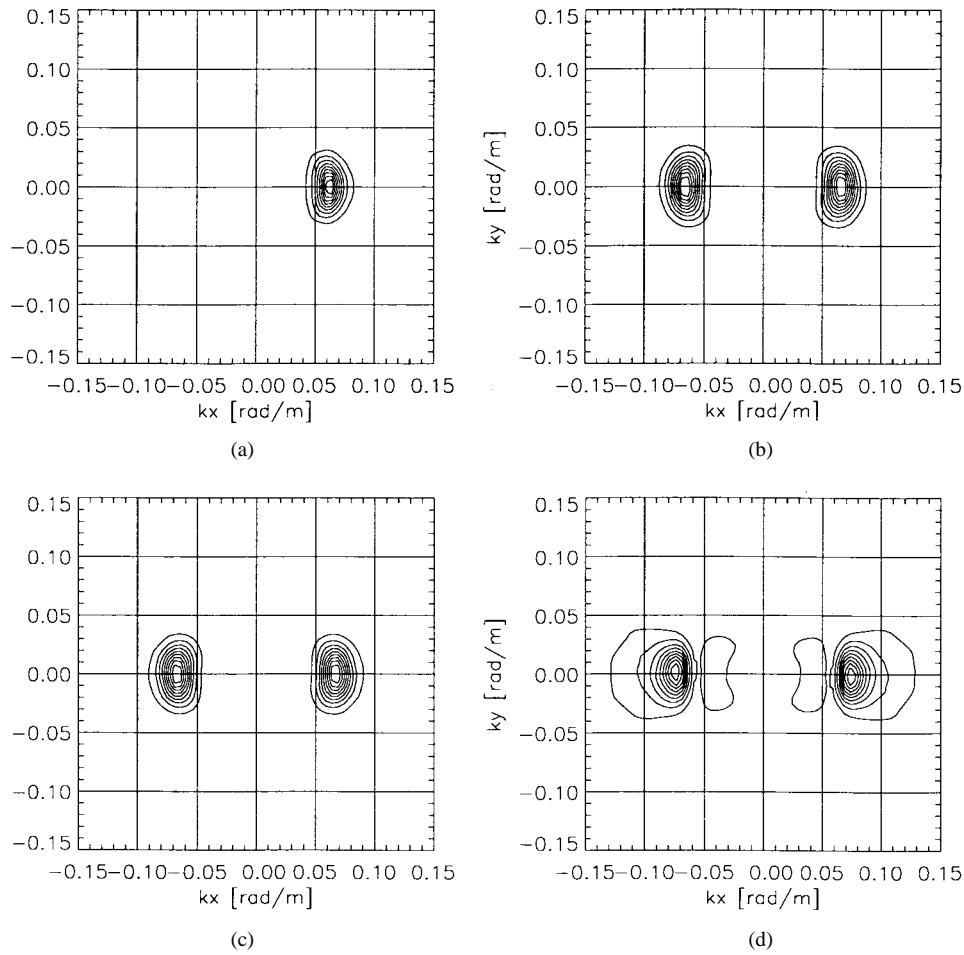
Fig. 6.   Same as Fig. 2, but with $\phi_p = 0°$ (azimuthally traveling waves).
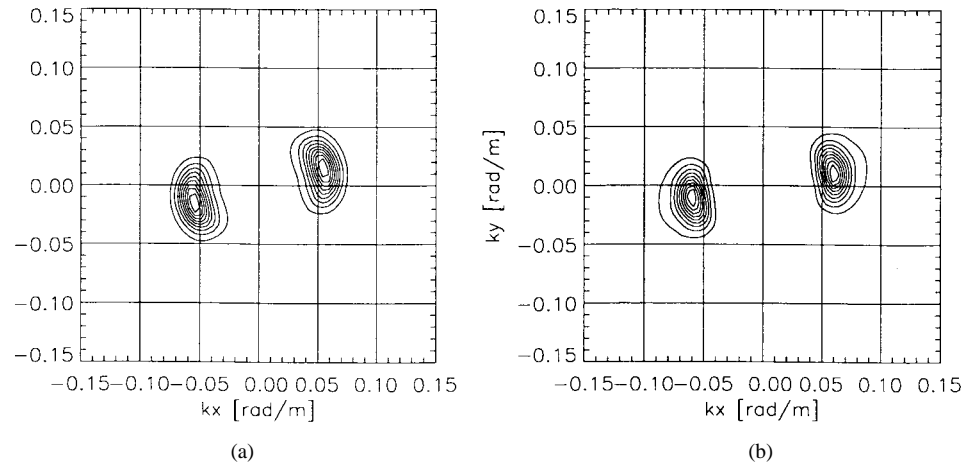

Fig. 7.   (a) AT-INSAR phase image spectrum simulated from the ocean wave spectrum plotted in Fig. 4(a) with the velocity bunching term omitted in (15). (b) Same as (a), but with the velocity term omitted.

conclude that the MTF affects the AT-INSAR phase image spectra in these simulations only very little.

G. AT-INSAR Interferogram Spectra

Lyzenga and Bennett [13] have derived an expression for the Fourier transform of the complex AT-INSAR image for an AN-INSAR operating in mode 2 (the two antennas emit and receive pulses). They call this spectrum "interferogram spectrum." By using our time dependent AT-INSAR model we can reproduce their result [28]. Lyzenga and Malinas [29] have analyzed AT-INSAR data which were acquired over the Gulf Stream by ERIM/NAWC P3 SAR system during the High Resolution Ocean Experiment in 1991 [29], and have calculated the modulus of the interferogram spectrum. This
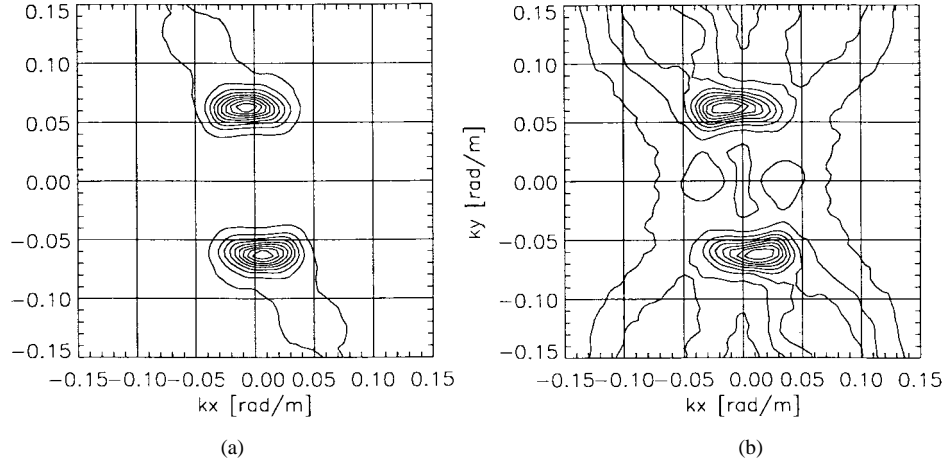
Fig. 8. AT-INSAR phase image spectra simulated from the ocean wave spectrum plotted in Fig. 2(a), with (a) $\Delta t = 0.200$ s and (b) $\Delta t = 0.225$ s. The scene coherence time is in both cases $\tau_s = 0.12$ s.
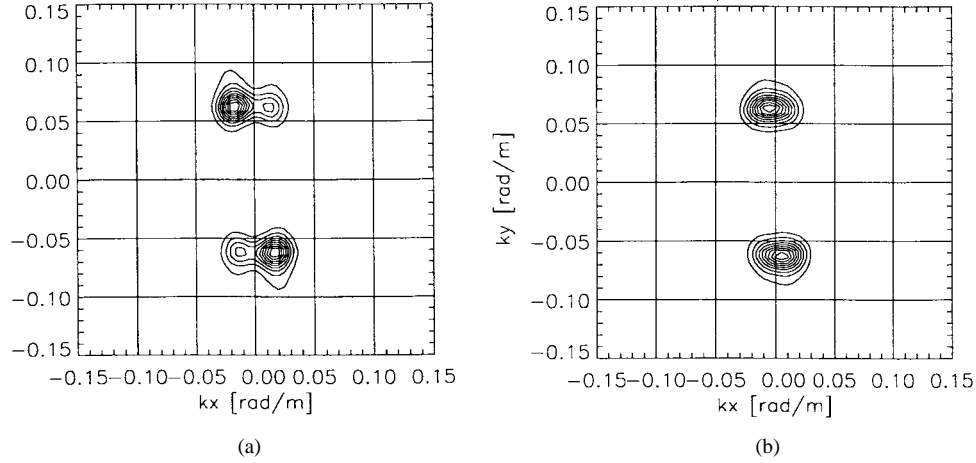

Fig. 9. AT-INSAR phase image spectra simulated from the ocean wave spectrum plotted in Fig. 2(a), with (a) $\tau_s = 0.03$ s and (b) $\tau_s = 0.04$ s. The time separation between the observations by the two antennas is in both cases 0.049 s.

modulus is not symmetric with respect to the k_y-axis, where k_y denotes the wavenumber in range direction, because the azimuthal cut-off acts as a bandpass filter, and the center of this filter is shifted in azimuthal direction. This shift can be explained briefly as follows. For an AT-INSAR operating in mode 2, the round-trip paths form the aft and fore antennas to the scattering element located at (x_0, y_0, z_0) are given by

$$R_1 = 2R + \frac{(x_0 - x + B)^2}{R} - 2\cos\theta z_0(\mathbf{x_0}, t)$$

and

$$R_2 = 2R + \frac{(x_0 - x - B)^2}{R} - 2\cos\theta z_0(\mathbf{x_0}, t)$$

respectively, where x denotes the coordinate in azimuthal direction in AT-INSAR image plane, and R the range distance. The signals received by the two antennas have a phase shift

$$\phi_s = k_i(R_2 - R_1) = \frac{4Bk_i(x - x_0)}{R} \tag{19}$$

where k_i denotes the wavenumber of the incoming electromagnetic wave. For simplicity we do not consider here the phase shift due to the motion of the scattering element. In this

case the expression for the AT-INSAR image intensity reads

$$I(\mathbf{x}) = \int \sigma(\mathbf{x_0}) \exp\left\{-\frac{\pi^2}{\rho_a^2}(x - x_0)^2\right\} \exp(j\phi_s) dx_0$$

$$= I_1(\mathbf{x}) \exp\left\{\frac{4jBk_ix}{R}\right\} \tag{20}$$

where $I_1(\mathbf{x})$ is given by

$$I_1(\mathbf{x}) = \int \sigma(\mathbf{x_0}) \exp\left\{-\frac{\pi^2}{\rho_a^2}(x - x_0)^2\right\}$$

$$\times \exp\left\{-\frac{4jBk_ix_0}{R}\right\} dx_0. \tag{21}$$

When $B = 0$, the formula $I_1(\mathbf{x})$ reduces to the expression of the conventional SAR image intensity for fixed scattering elements.

The Fourier transform of the AT-INSAR image intensity yields

$$I(\mathbf{x}) = \int I_1(\mathbf{x}) \exp\left\{\frac{4jBk_ix}{R}\right\} \exp(-jk_xx - jk_yy) dx dy$$

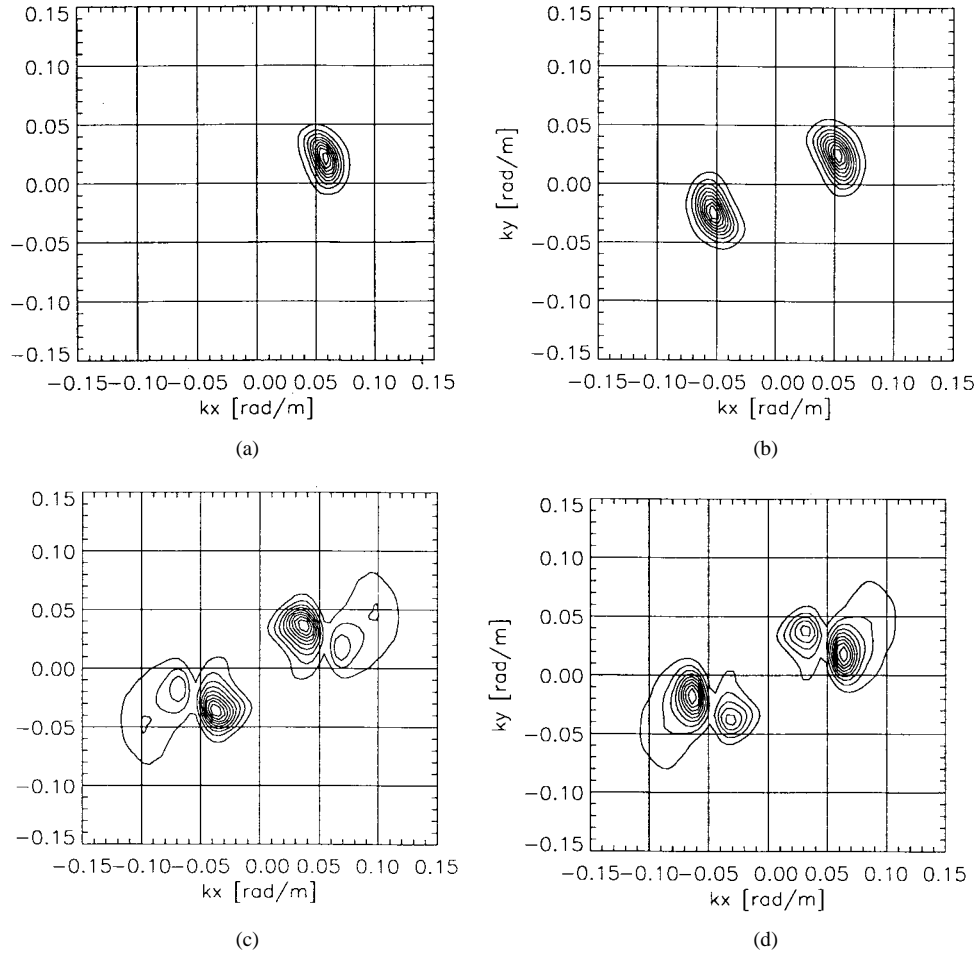$$= I_1\left(k_x - \frac{4Bk_i}{R}, k_y\right). \tag{22}$$

Fig. 10. (a) Ocean wave spectrum. (b) AT-INSAR phase image spectrum simulated from the ocean wave spectrum plotted in (a) with $R/V = 30$ s, (c) same as (b), but with $R/V = 80$ s, (d) same as (b), but with $R/V = 90$ s.

Therefore, as compared to conventional SAR image spectrum, the Fourier transform of the AT-INSAR image intensity (interferogram spectrum) is shifted in azimuthal direction by an amount equal to [13], [29]

$$k_x^{(m)} = 4Bk_i/R. \qquad (23)$$

As a consequence, the azimuthal cut-off wavenumber in the modulus of the interferogram spectrum is also shifted toward higher azimuthal wavenumbers. This azimuthal shift is proportional to the separation distance between the two antennas. However, this improvement of the imaging of ocean waves is limited by the condition that the time separation between the observations by the fore and aft antennas $(\Delta t = 2B/V)$ must be smaller than the scene coherence time (τ_s) in order to avoid distortion (see Section III-C).

We have simulated the modulus of the interferogram spectrum for a swell spectrum. In the simulations we have chosen the wavelength and the azimuthal angle of the dominant wave as 65 m and 0°, respectively, and the significant waveheight as $H_s = 1.7$ m. We have used the radar and flight parameters given in Table II with the exception of $2B$, which we have set here equal to 10 m. Note that in all these simulations
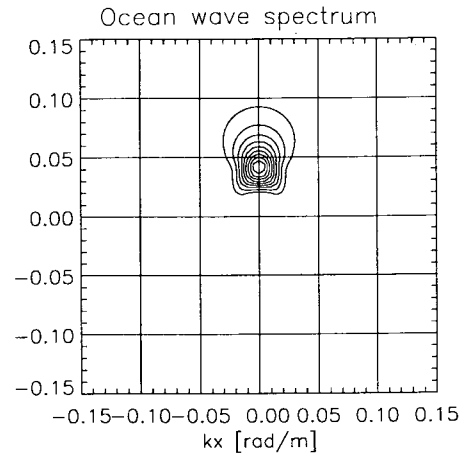

Fig. 11. Pierson–Moskowitz ocean wave spectrum for a wind speed of $U_{10} = 12$ m/s.

the scene coherence time was kept constant at $\tau_s = 0.11$ s. From Fig. 13(c) we see that the modulus of the interferogram spectrum is shifted in azimuthal direction by $k_x^{(m)} = 0.040$ rad/m, i.e., the center of the spectrum is shifted from $(0,0)$ to $(0.040, 0)$, which is in agreement with the theoretical value of $k_x^{(m)} = 0.035$ rad/m calculated from the (23). Our
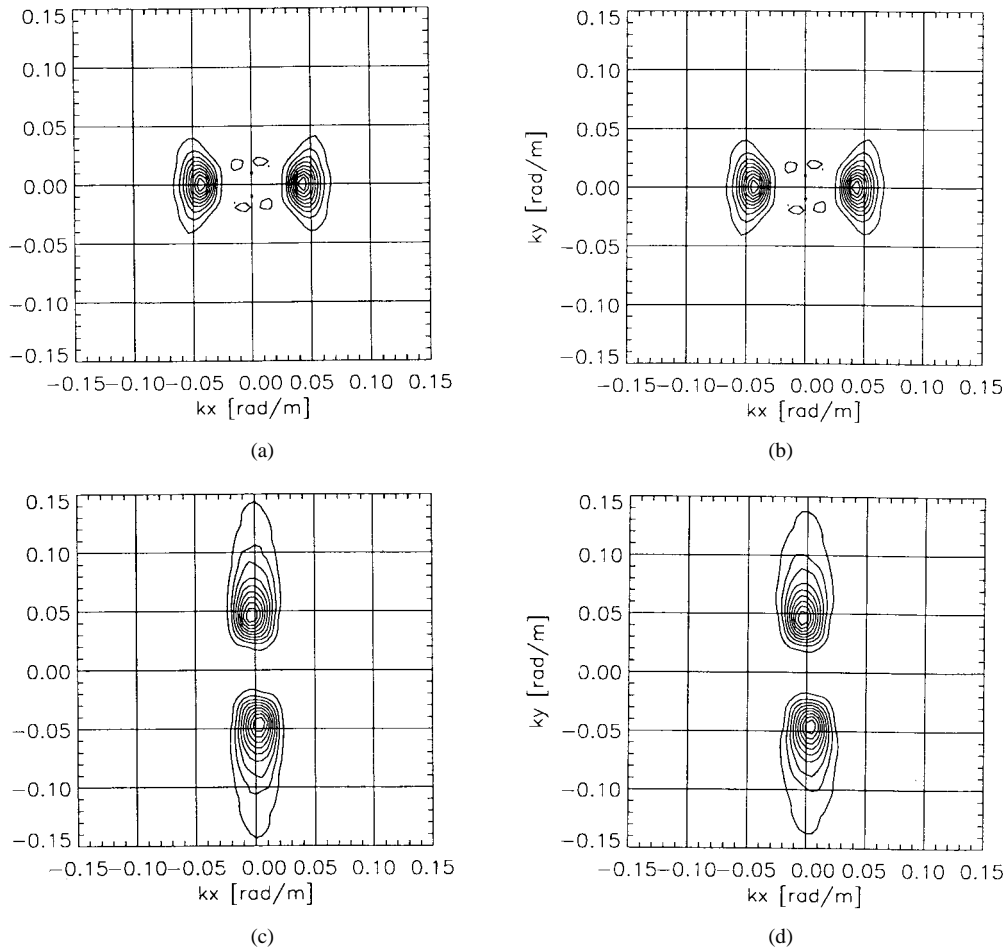
Fig. 12.   AT-INSAR phase image spectra simulated from the Pierson–Moskowitz spectrum shown in Fig. 11. The AT-INSAR phase image spectra plotted in (a) and (c) are calculated with a constant $\sigma(\mathbf{x_0})$ ($\mathrm{MTF} = 0$) and the ones plotted in (b) and (d) with the "theoretical" MTF. In (a) and (b) the dominant ocean wave propagates in azimuthal direction and in (c) and (d) in range direction.

simulation also show that both, the modulus of interferogram spectrum [Fig. 13(c)] and the AT-INSAR phase image spectrum [Fig. 13(d)], have the same bandwidth in the positive azimuthal wavenumber regime ($k_x > 0$). This bandwidth is larger than the bandwidth of the corresponding conventional SAR image spectrum [Fig. 13(b)]. Furthermore, we find in our simulations that the shift of the spectral peak toward the range axis is smaller in the modulus of the interferogram spectrum [Fig. 13(c)] and in the AT-INSAR phase image spectrum [Fig. 13(d)] than in the conventional SAR image spectrum [Fig. 13(b)].

IV. DISCUSSION AND CONCLUSION

In this paper we have extended the velocity bunching model for a conventional SAR to a velocity bunching model for an AT-INSAR. This model includes the modulation of the normalized radar cross section, velocity bunching, and degradation of the azimuthal resolution due to orbital acceleration associated with the long waves and due to the orbital velocity spread within the AT-INSAR resolution cell, which is parameterized by the scene coherence time. Using the Monte-Carlo method we have simulated the AT-INSAR imaging of a 2-D ocean surface wave field and have computed 2-D AT-INSAR phase

and amplitude image spectra for different ocean wave and radar parameters.

It is shown that velocity bunching contributes to the AT-INSAR imaging mechanism when the ocean waves have significant azimuthal components and small wavelengths and when the R/V ratio is large. In this case, an interference between the velocity term and the velocity bunching term in the mapping integral (15) may result in a splitting of the AT-INSAR phase image spectrum. Thus, in order to avoid the splitting of AT-INSAR phase image spectrum, we suggest to use small R/V ratio (e.g., $R/V < 80$ s) when imaging ocean waves by AT-INSAR.

In addition, we have simulated AT-INSAR imaging of ocean waves using different ocean wave-radar modulation transfer functions (MTFs). These simulations show that the AT-INSAR phase image spectra are quite insensitive to the MTF. On the other hand, the conventional SAR image spectra and the AT-INSAR amplitude image spectra as well as the modulus of AT-INSAR interferogram spectra are affected by this MTF which is a poorly known function. Thus, we conclude that it is better to use AT-INSAR phase image spectra for retrieving ocean wave spectra than to use a) AT-INSAR amplitude image spectra, b) the modulus of AT-INSAR interferogram spectra
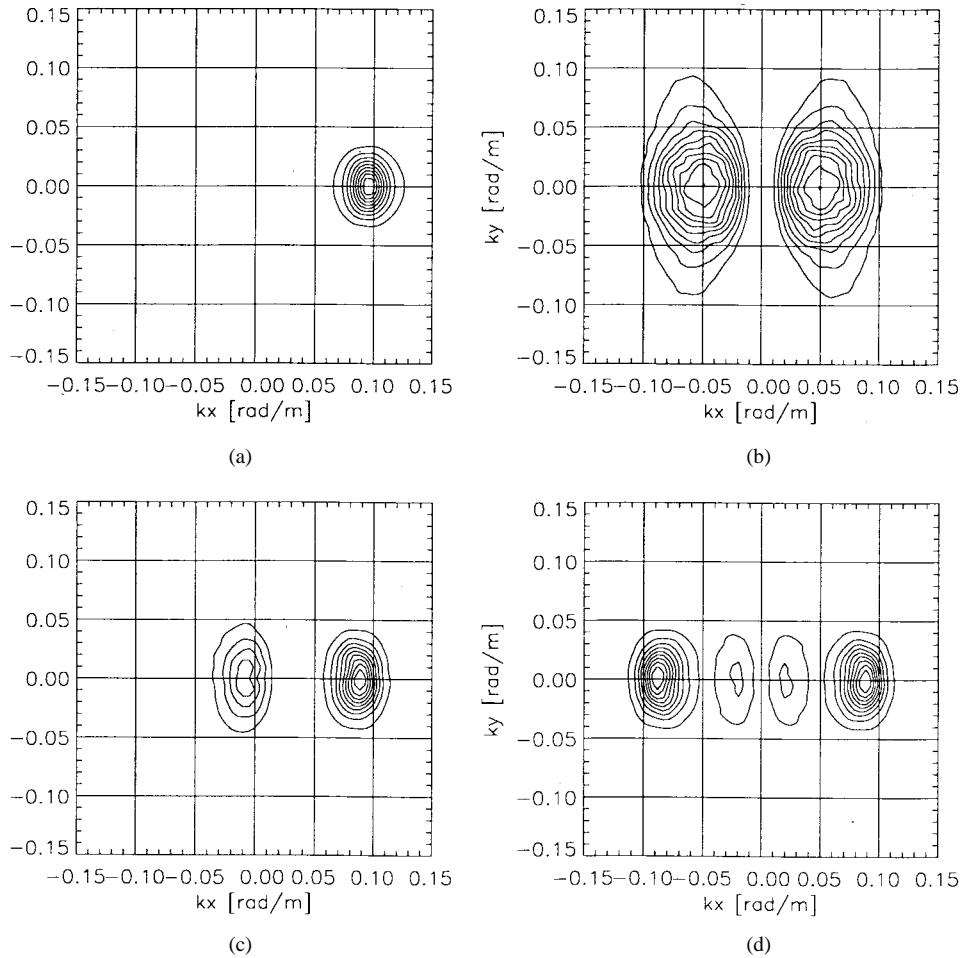
Fig. 13. (a) Ocean wave spectrum with $\phi_p = 0°$ (azimuthal traveling waves), (b) conventional SAR image spectrum, (c) modulus of the interferogram spectrum, and (d) AT-INSAR phase image spectrum simulated from the ocean wave spectrum shown in (a).

as discussed by Lyzenga and Bennett, or c) conventional SAR image spectra.

When applying AT-INSAR for measuring ocean wave spectra, the time separation between the two observations by the fore and aft antennas should be chosen smaller than the scene coherence time (τ_s), otherwise the signals received by the two antennas lose coherence and the AT-INSAR phase image spectra become distorted. A series of Monte-Carlo simulations carried out with different antenna separations and different scene coherence times confirms this conclusion.

Furthermore, we have calculated the modulus of interferogram spectrum as defined by Lyzenga and Bennett [13] using our AT-INSAR imaging model. Our results about the shift of the azimuthal cut-off wavenumber toward higher wavenumbers in the modulus of the interferogram spectrum are in agreement with results obtained by Lyzenga et al. [13], [29]. However, we want to point out that Lyzenga and Bennett's interferogram spectrum cannot be compared directly with the AT-INSAR phase and amplitude image spectra derived in this paper and in the papers of Marom et al. [10] and Shemer and Kit [15].

REFERENCES

[1] W. Alpers, D. B. Ross, and C. L. Rufenach, "On the detectability of ocean surface waves by real and synthetic aperture radar," *J. Geophys. Res.*, vol. 86, no. C7, pp. 6481–6489, July 1981.
[2] K. Hasselmann, R. K. Raney, W. J. Plant, W. Alpers, R. A. Shuchman, D. R. Lyzenga, C. L. Rufenach, and M. J. Tucher, "Theory of synthetic aperture radar ocean imaging: A MARSEN review," *J. Geophys. Res.*, vol. 90, no. C3, pp. 243–254, Mar. 1985.
[3] W. Alpers and C. Brüning, "On the relative improtance of motion-related contributions to the SAR imaging mechanism of ocean surface waves," *IEEE Trans. Geosci. Remote Sensing*, vol. GRS-24, pp. 873–885, Nov. 1986.
[4] C. Brüning, "The impact of the ocean wave-radar modulation transfer function on the inversion of ERS-1 SAR image spectra into ocean wave spectra," in *Proc. Int. Geosci. Remote Sens. Symp., (IGARSS'94)*, Pasadena, CA, 1994, pp. 2032–2034.
[5] A. Schmidt, V. Wismann, R. Romeiser, and W. Alpers, "Simultaneous measurements of the ocean wave-radar modulation transfer function at L, C and X bands from the research platform Nordsee," *J. Geophys. Res.*, vol. 100, no. C5, pp. 8815–8827, May 1995.
[6] R. M. Goldstein and H. A. Zebker, "Interferometric radar measurements of ocean surface currents," *Nature*, vol. 328, no. 20, pp. 707–709, Aug. 1987.
[7] R. M. Goldstein, T. P. Barnett, and H. A. Zebker, "Remote sensing of ocean currents," *Science*, vol. 246, pp. 1282–1285, Dec. 1989.
[8] L. Shemer, M. Marom, and D. Markan, "Estimates of currents in the nearshore ocean region using interferometric synthetic aperture radar," *J. Geophys. Res.*, vol. 98, no. C4, pp. 7001–7010, Apr. 1993.

[9] D. R. Thompson and J. R. Jensen, "Synthetic aperture radar interferometry applied to ship-generated internal waves in the 1989 Loch Linnhe experiment," *J. Geophys. Res.*, vol. 98, no. C6, pp. 10259–10269, June 1993.

[10] M. Marom, L. Shemer, and E. B. Thornton, "Energy density directional spectra of a nearshore wave field measured by interferometric synthetic aperture radar," *J. Geophys. Res.*, vol. 96, no. C12, pp. 22125–22134, Dec. 1991.

[11] R. Shuchman, A. Ochadlick, P. Cho, W. Dunlevy, J. Lyden, D. Lyzenga, and C. Wackerman, "Interferometric SAR measurements collected during the high resolution ocean experiment," in *Proc. Int. Geosci. Remote Sens. Symp. 1992 (IGARSS'92)*, Arlington, TX, 1992, pp. 458–461.

[12] A. L. Gray, M. W. A. van der Kooijm, K. E. Mattar, and P. J. Farris-Manning, "Progress in the development of the CCRS along-track interferometer," in *Proc. Int. Geosci. Remote Sens. Symp. 1994 (IGARSS'94)*, Pasadena, CA, 1994, pp. 2285–2287.

[13] D. R. Lyzenga and J. R. Bennett, "Estimation of ocean wave spectra using two-antenna SAR systems," *IEEE Trans. Geosci. Remote Sens.*, vol. 29, pp. 463–465, May 1991.

[14] A. S. Milman, A. O. Scheffler, and J. R. Bennett, "Ocean imaging with two-antenna radars," *IEEE Trans. Antennas Propagat.*, vol. 40, pp. 597–605, June 1992.

[15] L. Shemer and E. Kit, "Simulation of an interferometric synthetic aperture radar imagery of ocean system consisting of a current and a monochromatic wave," *J. Geophys. Res.*, vol. 96, no. C12, pp. 22063–22073, Dec. 1991.

[16] L. Shemer, "An analytical presentation of the monochromatic ocean wave image by a regular or an interferometric synthetic aperture radar," *IEEE Trans. Geosci. Remote Sensing*, vol. 33, pp. 1008–1013, July 1995.

[17] ———, "The effect of the real aperture radar modulation on the interferometric SAR imagery of ocean waves," in *Proc. Int. Geosci. Remote Sens. Symp. 1993 (IGARSS'93)*, Tokyo, Japan, 1993, pp. 22–24.

[18] R. E. Carande, "Estimating ocean coherence time using daul-baseline interferometric synthetic aperture radar," *IEEE Trans. Geosci. Remote Sensing*, vol. 32, pp. 847–854, July 1994.

[19] W. Alpers and C. L. Rufenach, "The effect of orbital motions on synthetic aperture radar imagery of ocean waves," *IEEE Trans. Antennas Propagat.*, vol. AP-27, pp. 685–690, Sept. 1979.

[20] D. R. Lyzenga, "An analytic representation of the synthetic aperture radar image spectrum for ocean waves," *J. Geophys. Res.*, vol. 93, no. C11, pp. 13859–13865, Nov. 1988.

[21] D. P. Kasilingam and O. H. Shemdin, "Theory for synthetic aperture radar imaging of the ocean surface: With application to the tower ocean wave and radar dependence experiment on focus, resolution, and wave height spectra," *J. Geophys. Res.*, vol. 93, no. C11, pp. 13837–13848, Nov. 1988.

[22] W. J. Plant, "Reconciliation of theories of synthetic aperture radar imagery of ocean waves," *J. Geophys. Res.*, vol. 97, no. C5, pp. 7493–7501, May 1992.

[23] ———, personal communication, 1995.

[24] C. Brüning, W. Alpers, L. F. Zambresky, and D. G. Tilley, "Validation of a synthetic aperture radar ocean wave imaging theory by the shuttle imaging radar-B experiment over the North sea," *J. Geophys. Res.*, vol. 93, no. C12, pp. 15403–15425, Dec. 1988.

[25] W. Alpers, "Monte Carlo simulations for studying the relationship between ocean wave and synthetic aperture radar image spectra," *J. Geophys. Res.*, vol. 88, no. C3, pp. 1745–1759, Mar. 1983.

[26] C. Brüning, W. Alpers, and K. Hasselmann, "Monte-Carlo simulation studies of the nonlinear image of a two-dimensional surface wave field by SAR," *Int. J. Remote Sensing*, vol. 11, no. 10, pp. 1695–1727, 1990.

[27] C. Brüning, R. Schmidt, and W. Alpers, "Estimation of the ocean wave-radar modulation transfer function from synthetic aperture radar imaging," *J. Geophys. Res.*, vol. 99, no. C5, pp. 9803–9816, May 1994.

[28] M. Bao, "On the imaging of a two-dimensional ocean surface wave field by an along-track interferometric synthetic aperture radar," Ph.D. Dissertation, The University of Hamburg, Germany, pp. 69–72, 1995.

[29] D. R. Lyzenga and N. P. Malinas, "Airborne radar measurements of coastal ocean currents and waves," in *Proc. Second Thematic Conf. Remote Sens. Marine Coastal Environ.*, New Orleans, LA, 1994, pp. 379–388.

Mingquan Bao was born in Hangzhou, P.R.C., on Oct. 27, 1962. He received the B.S. and M.S. degrees in electrical engineering from the University of Zhejiang, P.R.C., in 1985 and 1988, respectively. He received the Ph.D. degree (Dr.rer.nat.) from the University of Hamburg, Germany, in 1995.

From 1988 to 1992, he was a Research Assistant in the Second Institute of Oceanography, P.R.C. Presently, he is with the Institute of Oceanography at the University of Hamburg, Germany. His research interests include the oceanographic application of conventional and interferometric SAR, radar backscattering from the ocean surface, and signal processing.

Claus Brüning was born in Bremerhaven, Germany, on Feb. 12, 1953. He received the diploma degree in meteorology and the Ph.D. degree (Dr.rer.nat.) from the University of Hamburg, Hamburg, Germany, in 1982 and 1987, respectively.

From 1982 to 1987, he was in the field of remote sensing at the Max Planck Institute for Meteorology, Hamburg, and from 1987 to 1990, he was with the European Centre for Medium Range Weather Forecasts (ECMWF), Reading, U.K., where he was involved in the Tropical Ocean and Global Atmosphere (TOGA) project. From 1991 to 1995, he was with the University of Hamburg, where he was engaged in assimilating satellite data into wave prediction models. Since March 1995, he has been with the European Commission in the Environment and Climate programme of the Directorate General for Research and Technology, serving as a Scientific Officer.

Werner Alpers received the diploma in physics (Dipl.-Phys.) from the University of Hamburg, Hamburg, Germany, in 1962, the M.S. degree in physics from the University of Wisconsin, Madison, in 1964, and the Ph.D. degree (Dr.rer.nat.) in theoretical physics (elementary particle physics) from the University of Hamburg in 1967.

From 1968 to 1970, he worked in space physics at the European Space Research Institute (ESRIN), Frascati, Italy, and from 1970 to 1973 at the Max Planck Institute for Physics and Astrophysics, Munich, Germany. In 1973, he became engaged in remote sensing of the ocean and worked from 1973 to 1985 at the University of Hamburg and the Max Planck Institute for Meteorology, Hamburg. From 1985 to 1989, he was Professor in the Department of Physics and Electrical Engineering, University of Bremen, Germany, and since 1989, he has been full Professor at the Institute of Oceanography, University of Hamburg, leading the research group "Satellite Oceanography." Since 1973, he has been engaged in microwave remote sensing of the ocean by using laboratory, airborne, and spaceborne sensors. Furthermore, he has developed theoretical models for describing the imaging of ocean surface waves, internal waves, and underwater bottom topography by synthetic aperture radars. Recently, his research activities focused on extracting information on the marine boundary layer from spaceborne synthetic aperture radar images of the ocean surface. He was a Principal Investigator for the Shuttle Imaging Radar B (SIR-B mission), and is currently a Principal Investigator for ERS-1/2 and for the Shuttle Imaging Radar C/X-SAR missions. He has been active in several advisory committees of the German Ministry of Science and Technology, the German Science Foundation, and the European Space Agency for defining earth observation satellite missions. In particular, he has been involved in ESA's ERS-1, ERS-2 and Envisat projects as an advisor. He has authored or co-authored more than 100 papers dealing with different aspects of microwave remote sensing of the ocean.Z